JOM Journal of Optical Microsystems

RESEARCH PAPER

Four-wave mixing in silicon nanophotonic waveguides and microring resonators: influence of two-photon absorption

Arnab Goswami, Yash Raj, and Bijoy Krishna Das*
IIT Madras, Center for Programmable Photonic Integrated Circuits and Systems, Department of Electrical Engineering, Chennai, Tamil Nadu, India

ABSTRACT. Four-wave mixing (FWM) in silicon photonics offers promising applications in optical signal processing, wavelength conversion, and quantum photonics, necessitating a comprehensive understanding of its underlying physics and limitations. Stimulated four-wave mixing in silicon photonic wire waveguides has been investigated theoretically by considering two-photon absorption, free carrier absorption, and free carrier dispersion, etc., operating near $\lambda \sim 1550$ nm. It has been shown that these effects severely degrade the performance when operating at higher pump power levels. We present exact numerical calculations of idler wavelength conversion efficiency and bandwidth taking into account the abovementioned nonlinearities, to show the effects of various parameters within the waveguide structure. We extended to investigate silicon photonic microring resonators in terms of the four-wave mixing performance of high-Q-value microring resonators, which are very promising as photon sources (spontaneous four-wave mixing) for large-scale quantum photonic circuits. Our analysis illustrates the limitations of analytical models in describing FWM in ring resonator behavior at a moderate input power level, necessitating a rigorous numerical approach. Experimentally, we demonstrate stimulated FWM ($1525\ \text{nm} \leq \lambda_p \leq 1575\ \text{nm}$) in a silicon photonic wire with a cross-section of $500\ \text{nm} \times 220\ \text{nm}$ and with a small waveguide length of 2 mm. The idler-to-signal conversion efficiency of about −35 dB has been measured for an approximate launched pump power of 30 mW. The conversion efficiency is improved further in the microring resonator as predicted by the simulation results.

Keywords: silicon photonics; nonlinear optics; stimulated four-wave mixing; microring resonator

Paper 24009SS received Mar. 1, 2024; revised Sep. 6, 2024; accepted Sep. 16, 2024; published Oct. 16, 2024.

1 Introduction

Silicon photonics, compatible with complementary metal-oxide-semiconductor technology, enables a wide range of applications, from high-speed communications to quantum information processing.[1] Four-wave mixing (FWM) in silicon photonic waveguides and microring resonators (MRRs) has gained significant interest due to its potential for various applications in photonic signal processing.[2] The ability to achieve efficient and controlled FWM processes within these silicon structures opens up possibilities for advanced wavelength conversion[3] and the generation of quantum photonic sources.[4]

*Address all correspondence to Bijoy Krishna Das, bkdas@ee.iitm.ac.in

Early research primarily focused on optimizing FWM efficiency by minimizing group velocity dispersion (GVD) for broadband FWM operations through various techniques such as geometry optimizations and intermodal phase matching. Foster et al.[5] demonstrated broadband frequency conversion via FWM in a dispersion-engineered silicon waveguide with a height of 300 nm and a width ranging from 500 to 750 nm. They used the fourth-order dispersion to demonstrate frequency conversion from 1477 to 1672 nm with conversion efficiency (CE) of −12 dB. However, their analysis is restricted to small-gain limit, where the nonlinear losses of two-photon absorption (TPA) and free carrier absorption (FCA) are neglected. These losses are responsible for limiting the CE in the high optical power regime. In the small-gain limit, the CE is quadratically dependent on pump power, but the conversion bandwidth is independent of it. To achieve frequency conversion over a large spectral range, Signorini et al.[6] used higher-order modes of optical waveguide to achieve frequency conversion over a large spectral range. When an intermodal combination is excited using pump and signal, the spectral position of the phase matching is moved far from the pump wavelength due to larger differences in effective indices of the involved modes, allowing for wavelength conversion over a large spectral distance. Due to mode field profile mismatch, in the case of intermodal FWM, its CE is lower as compared with that of intramodal FWM. The on-chip idler generations deviated from quadratic dependence on the pump power beyond the 0.5-mW pump power. However, while exploring the dynamics of stimulated FWM in silicon waveguides and MRRs, it is essential to consider the influence of nonlinear processes such as TPA, FCA, and free carrier dispersion (FCD).[7] The refractive index and propagation loss are affected by the higher power in the waveguide. These factors play a crucial role in shaping the FWM dynamics and ultimately impact the CE and bandwidth of the process. In a high optical power regime, nonlinear effects such as TPA and FCA limit the CE of FWM. Shayan et al.[8] have demonstrated enhancement in CE by active carrier removal using PIN junction in the cross-section of the waveguide. Using active carrier removal, they showed improvement of CE by 5 to 6 dB in the rib waveguide and 8 to 10 dB in the MRR. Active carrier removal shows a larger enhancement in CE by reducing the free carrier lifetime from the waveguide, resulting in reduced nonlinear effects. However, a detailed theoretical and numerical analysis is required to fully understand and optimize this approach. Borghi et al. [9] demonstrated enhanced FWM in a coupled silicon MRR structure. By carefully aligning the inter-resonator phase to either 0 or π, they achieved a 7-dB increase in CE compared with individual resonators. This enhancement was attributed to constructive interference between the signal waves generated in each MRR, leading to amplified signal fields and improved FWM. However, this study does not investigate the trend of CE with field enhancement in the MRRs.

Previous studies have primarily focused on stimulated FWM in waveguides and resonators operating under low-power conditions. While analytical models have been employed to investigate FWM in MRRs, their accuracy diminishes at higher pump powers due to the influence of nonlinear effects. This paper presents a comprehensive numerical study of stimulated FWM in both straight waveguides and MRRs, incorporating the impact of TPA, FCA, and FCD. By solving the coupled equations governing the FWM process, we quantify the effects of various parameters on CE and bandwidth. Our results underscore the limitations of analytical approaches in modeling high-power FWM in MRRs and emphasize the necessity of rigorous numerical simulations. In Sec. 2, the theoretical background of stimulated FWM is discussed. Section 3 provides a comprehensive discussion of the nonlinear effects encountered in these waveguides followed by numerical simulations of stimulated FWM, focusing on both straight waveguides and ring resonators. In Sec. 4, the experimental results are provided to support the empirical validation of the theoretical and numerical findings followed by a conclusion and summary.

2 Background Theory

The induced polarization (P) in a medium depends on the susceptibility (χ) of the material and the power of the incident optical field (E). In the frequency domain, total polarization is expressed as

$$P = \epsilon_0 \chi^{(1)} E + \epsilon_0 \chi^{(2)} E^2 + \epsilon_0 \chi^{(3)} E^3 + \ldots . \quad (1)$$

In the right-hand side of Eq. (1), the first term ($\epsilon_0\chi^{(1)}E$) is the linear polarization (P_L) and the rest of the terms contribute to the nonlinear polarization (P_{NL}) of the medium. Being centrosymmetric, all even order terms in the above equation are zero in general for silicon. Therefore, the lowest-order nonlinearity in silicon comes from the third-order susceptibility ($\chi^{(3)}_{Si} = 1.9 \times 10^{-19}\ \mathrm{m}^2/\mathrm{V}^2$)

$$P^3_{\mathrm{NL}} = \epsilon_0\chi^{(3)}\vdots\mathrm{EEE}. \tag{2}$$

Therefore, the refractive index becomes a function of the intensity (I) of the optical waves. The total refractive index (n) can be defined as

$$n = n_o + n_2 I, \tag{3}$$

where n_o is the linear refractive index and n_2 is the Kerr nonlinear coefficient, described by[10]

$$n_2 = \frac{3\chi^{(3)}}{4n_o^2\epsilon_o c}. \tag{4}$$

When light waves propagate through a medium, the excitation of nonlinear polarization generates new frequencies, as governed by the wave equation:

$$\nabla^2 E_m + n^2\beta_m^2 E_m = -\mu_0\omega_m^2 P_{NL}, \tag{5}$$

where $\beta_m = \omega_m/c$ is the propagation constant. In the spontaneous FWM process, when a highly intense pump (ω_p) propagates through a medium with sufficient $\chi^{(3)}$, correlated photon pairs, signal (ω_s), and idler (ω_i) waves are generated in accordance with both energy conservation ($2\omega_p = \omega_s + \omega_i$) and momentum conservation ($2\beta_p = \beta_s + \beta_i$). This is depicted schematically in Fig. 1. Due to its low generation efficiency, the detection of photon pairs produced via spontaneous FWM needs the use of single-photon detectors. Conversely, in the classical process as shown in Fig. 2, a signal wave (ω_s) is deliberately stimulated alongside intense pump waves (ω_p) to generate stronger idler waves, which can be detected using an optical spectrum analyzer. The efficiency observed in the stimulated process directly relates to the efficiency of the spontaneous process. Hence, the stimulated FWM process has been investigated in detail.

Due to the highly intense pump, other nonlinear terms such as self-phase modulation (SPM) and cross-phase modulation (XPM) will modify the phase matching condition and the generation of idler will be affected. Considering the waves are propagating in the z directions, the electric field (E_m) can be written in terms of the amplitude A_m and waveguide mode ($\phi_m(x, y)$) as follows:

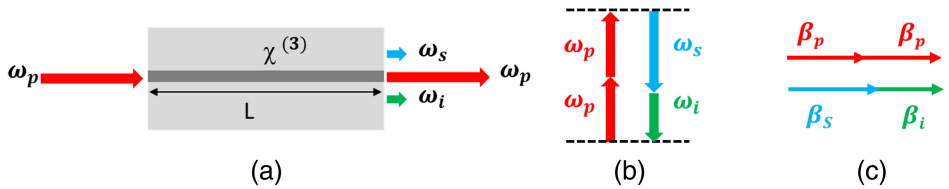

Fig. 1 Schematic view of (a) spontaneous FWM in a $\chi^{(3)}$ waveguide of length L, (b) energy conservation, and (c) momentum conservation.

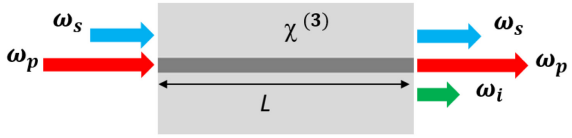

Fig. 2 Schematic view of stimulated FWM.

$$E_m = A_m(z)\phi_m(x,y)e^{j\beta_m z}. \tag{6}$$

For the FWM process, we considered a silicon photonic waveguide with the excitation of single polarization (TE-like). Consequently, all interacting waves are assumed to have the same polarization. In the presence of waveguide loss (α), the coupled equations between pump (A_p), signal (A_s), and idler (A_i) field amplitudes can be written as[10]

$$\frac{\partial A_p}{dz} = -\frac{\alpha_p}{2}A_p + j\gamma_p[|A_p|^2A_p + 2(|A_s|^2 + |A_i|^2)A_p + 2A_p^*A_sA_ie^{j\Delta\beta z}], \tag{7}$$

$$\frac{\partial A_s}{dz} = -\frac{\alpha_s}{2}A_s + j\gamma_s[|A_s|^2A_s + 2(|A_p|^2 + |A_i|^2)A_s + A_p^2A_i^*e^{-j\Delta\beta z}], \tag{8}$$

$$\frac{\partial A_i}{dz} = -\frac{\alpha_i}{2}A_i + j\gamma_i[|A_i|^2A_i + 2(|A_p|^2 + |A_s|^2)A_i + A_p^2A_s^*e^{-j\Delta\beta z}], \tag{9}$$

where γ_m and $\Delta\beta$ is given by

$$\gamma_m = \frac{2\pi n_2}{\lambda_m A_{\text{eff}}}, \tag{10}$$

$$\Delta\beta = \beta_s + \beta_i - 2\beta_p. \tag{11}$$

A_{eff} is the effective mode area. The generation of idler waves is characterized by the power CE as

$$\eta = \frac{P_i^{\text{out}}}{P_s^{\text{in}}} = \frac{|A_i^{\text{out}}|^2}{|A_s^{\text{in}}|^2}, \tag{12}$$

where P_i^{out} is the generated idler power at the output and P_s^{in} is the signal power at the input. Along with efficiency, another important factor to consider is the bandwidth of FWM for a fixed input pump power, where the CE remains within 3 dB from its peak.

3 Numerical Simulations

CE improves as the input pump power increases in the waveguide. However, as the power increases, along with Kerr nonlinearity, other significant mechanisms come into play within silicon. The cumulative energy of two photons at 1550 nm ($2E_{\text{photon}} = 2 \times 0.8$ eV $= 1.6$ eV) overcomes the silicon bandgap ($E_g^{\text{Si}} = 1.12$ eV), leading to optical power absorption. At high power levels, TPA occurs and results in the generation of free carriers and heat. The generated heat increases the refractive index of silicon ($dn/dT = 1.86 \times 10^{-4}$/K), while free carriers alter the refractive index and optical absorption of the medium through FCD and FCA. The nonlinear loss can be expressed as [11]

$$\Delta\alpha_{\text{NL}} = \alpha_{\text{TPA}} + \alpha_{\text{FCA}}, \tag{13}$$

$$\alpha_{\text{TPA}} = \beta_{\text{TPA}} \cdot \left(\frac{P}{A_{\text{eff}}}\right), \tag{14}$$

$$\alpha_{\text{FCA}} = \frac{\tau_{fc}\beta_{\text{TPA}}\sigma}{2h\nu} \cdot \left(\frac{P}{A_{\text{eff}}}\right)^2, \tag{15}$$

P is the power flow inside the waveguide. β_{TPA}, σ, τ_{fc}, h, and ν are the TPA coefficient, FCA cross-section, free carrier lifetime, Planck constant, and light frequency, respectively. Similarly, the nonlinear refractive index can be expressed as [12]

$$\Delta n_{\text{NL}} = n_{\text{Kerr}} + n_{\text{FCD}} + n_{\text{Thermal}}, \tag{16}$$

$$n_{\text{FCD}} = -8.25 \times 10^{-16}\lambda^2 \cdot \frac{\beta_{\text{TPA}}\tau_{fc}}{2h\nu} \cdot \left(\frac{P}{A_{\text{eff}}}\right)^2, \tag{17}$$

$$n_{\text{Thermal}} = \frac{dn_{\text{eff}}}{dT} \cdot \frac{\beta_{\text{TPA}}\tau_{\text{th}}}{\rho C} \cdot \left(\frac{P}{A_{\text{eff}}}\right)^2, \tag{18}$$

Table 1 Parameter used for nonlinear effects in silicon.

β_{TPA}	6.7×10^{-12} m/W	13
τ_{fc}	1 ns	12
σ	1.97×10^{-21} m^2	13
n_2	6×10^{-18} m^2/W	14
τ_{th}	1 μs	12
C	705 J/kg.K	15
ρ	2.3×10^3 kg.m^{-3}	15

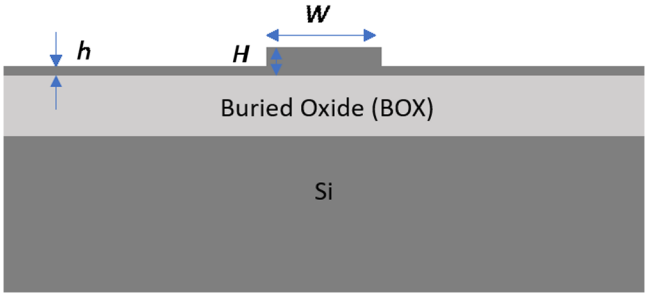

Fig. 3 Cross-section of a typical SOI waveguide; W, waveguide width; h, slab height; and H device layer thickness.

where τ_{th}, ρ, and C are the thermal dissipation time, density of silicon, and thermal capacity, respectively. $\frac{dn_{\text{eff}}}{dT}$ is the thermo-optic temperature coefficient of the waveguides whose effective index is n_{eff}. For the simulation of the nonlinear phenomena in the silicon waveguides, the following parameters (see Table 1) are used unless otherwise specified.

For waveguide design, a silicon-on-insulator (SOI) platform has been chosen, with specific layer dimensions: a device layer thickness of 220 nm, a buried oxide (BOX) layer thickness of 2 μm, and a silicon handle layer thickness of 700 μm. The upper cladding material is chosen as air. The cross-section of a typical SOI waveguide is shown in Fig. 3. The TPA and FCA-induced nonlinear losses have been plotted in Fig. 4a for a waveguide width (W) of 500 nm and slab height (h) of 0 nm. This choice of strip geometry ($h = 0$ nm) helps to achieve a lower effective area ($A_{\text{eff}} = 0.14$ μm^2), which results in higher nonlinearity. It is evident from Eqs. (14) and (15)

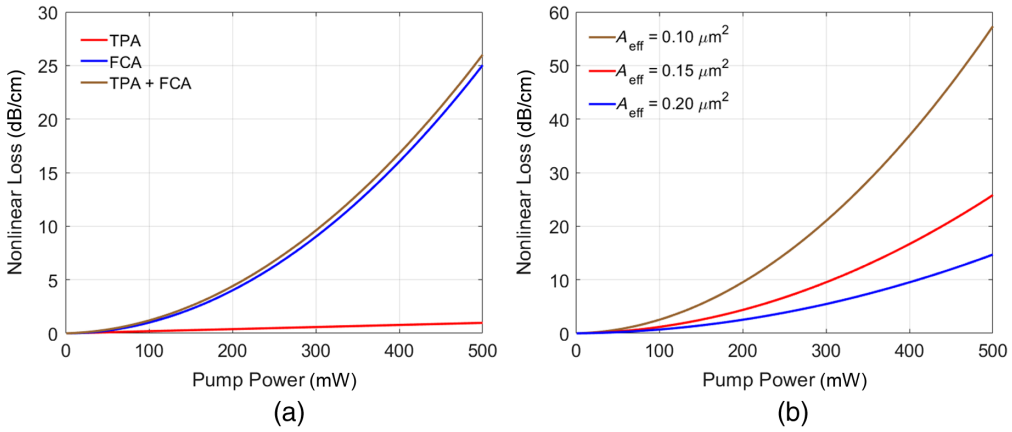

Fig. 4 (a) Nonlinear loss contribution for different processes against pump power for a fixed waveguide geometry ($W = 500$ nm, $h = 0$ nm) and (b) total nonlinear loss for different effective areas of the mode.

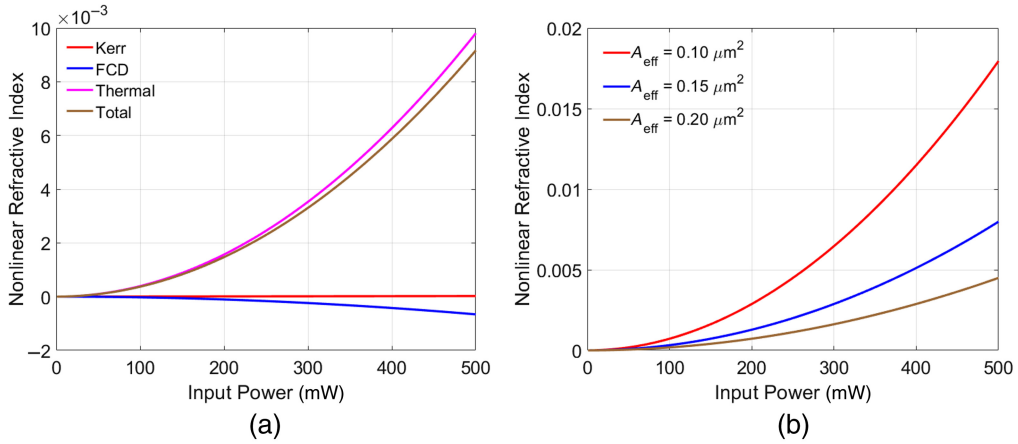

Fig. 5 (a) Nonlinear refractive index for different processes against pump power for a fixed waveguide geometry ($W = 500$ nm, $h = 0$ nm) and (b) total nonlinear refractive index for different effective areas of the mode.

that TPA loss depends on the intensity of the pump, whereas FCA loss depends on the square of the intensity. As the input power increases beyond 20 mW, the FCA loss dominates over the TPA loss, and at the higher input power, the total nonlinear loss comes majorly from the FCA effect. At an input power of 500 mW, the total nonlinear loss can exceed 25 dB/cm. The overall nonlinear loss is governed by the effective area, depending on the waveguide geometry. For instance, when the effective area increases from 0.10 to 0.20 μm^2, as calculated in Fig. 4(b), the overall nonlinear loss decreases by 40 dB/cm at 500 mW of optical power. In addition to losses, the refractive index of the medium is modified at high power levels. Figure 5(a) illustrates the individual contributions of each effect to the refractive index. While the refractive index increases through the Kerr effect and thermal effect, FCD reduces the refractive index. Nevertheless, at high power, thermal effects result in an overall positive change in the refractive index. Figure 5(b) represents the cumulative refractive changes for various effective areas. However, as the free carrier-induced refractive index change has a negligible effect on the phase matching condition,[7] the nonlinear loss and Kerr nonlinearity have been considered for the simulation of the stimulated FWM process.

The CE and bandwidth of the stimulated FWM process depend on several important parameters such as input pump power, waveguide propagation loss, and waveguide dispersion. In the following sections, the impact of stimulated FWM on different parameters is numerically simulated using MATLAB, based on previous theoretical analysis.

3.1 Straight Waveguide

For the simulations, a waveguide geometry of 500 nm × 220 nm with air as top cladding has been considered. The pump is chosen at 1550 nm. To get more insight into the impact of pump power and waveguide length, initially, the phase-matched condition ($\Delta\beta = 0$) has been considered. The CE with different pump power has been calculated in Fig. 6(a) for different lengths (L) of the waveguides. The linear propagation loss is assumed to be 5 dB/cm following the in-house silicon photonic fabrication technology at the Center for NEMS and Nano-Photonics (CNNP), IIT Madras. Across different waveguide lengths, the CE reaches a saturation point at higher power levels due to the prevailing nonlinear losses. However, it is worth noting that for a waveguide length of 5 cm, the CE is lower compared with that of a 2-cm long waveguide. This is attributed to the interplay between the linear propagation loss and generation of idler over the lengths. Nowadays, commercial silicon photonic foundries offer waveguide loss of around 1 dB/cm, the CE versus pump power has been calculated in Fig. 6(b) for a propagation loss of 1 dB/cm. The overall CE shows improvement across all lengths, and the results are comparable for different waveguide lengths at higher pump power. Therefore, it is important to investigate the CE along the length of the waveguide for different pump power levels at the input. Figure 7(a) depicts the CE across varying waveguide lengths for different power levels, assuming a linear propagation loss of 5 dB/cm. Beyond a certain waveguide length, the CE experiences a rapid decline, primarily due to losses becoming the limiting factor. It is worth highlighting that

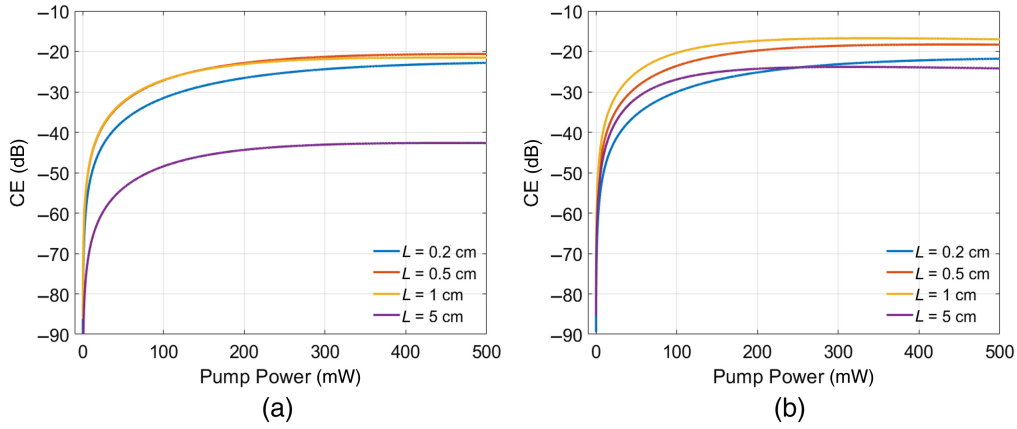

Fig. 6 (a) CE versus pump power for different lengths of waveguides for linear propagation loss of (a) 5 dB/cm and (b) 1 dB/cm.

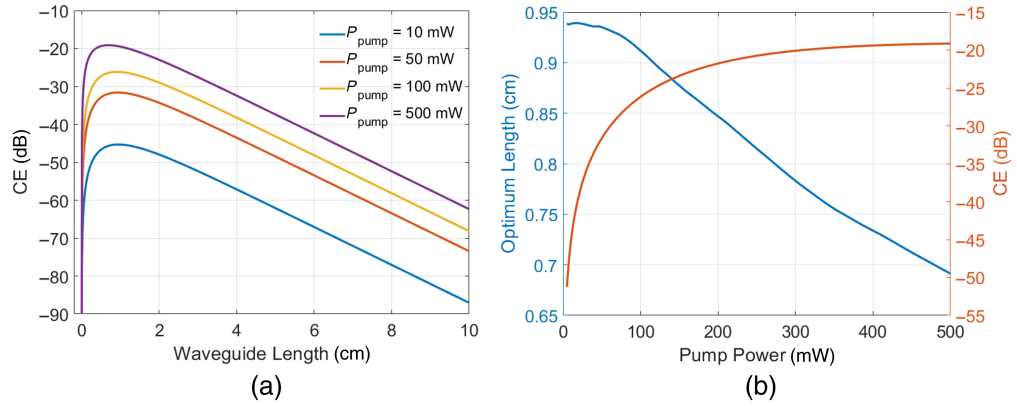

Fig. 7 (a) CE with waveguide length for different pump powers and (b) optimum waveguide length and corresponding CE with pump power variation for a propagation loss of 5 dB/cm.

the optimal waveguide length decreases as the pump power increases. The optimum waveguide length and the corresponding CE for different pump powers have been calculated as shown in Fig. 7(b). A similar effect of CE with respect to waveguide length has been simulated for a linear propagation loss of 1 dB/cm as shown in Fig. 8(a). However, after reaching the maximum CE at a specific waveguide length, the CE gradually diminishes along the waveguide's length. Therefore, the optimum waveguide length and its corresponding CE have been plotted in Fig. 8(b) against

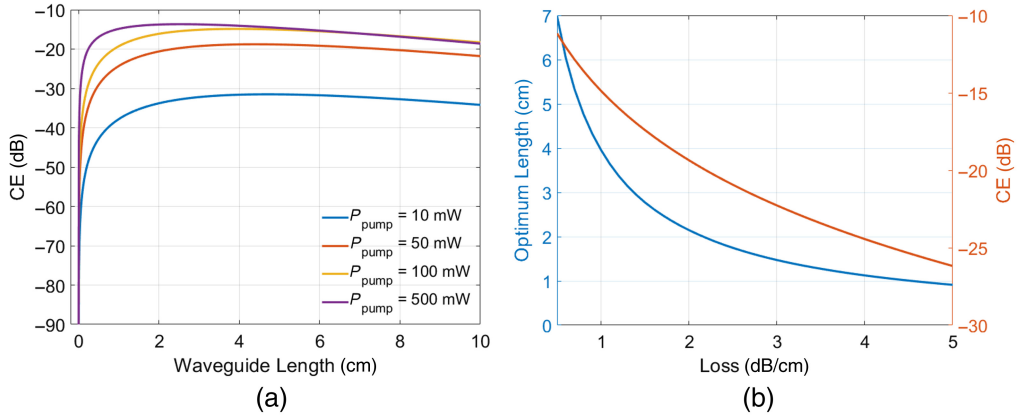

Fig. 8 (a) CE with waveguide length for different pump power with a propagation loss of 1 dB/cm and (b) optimum waveguide length and corresponding CE with propagation loss for a pump power of 100 mW.

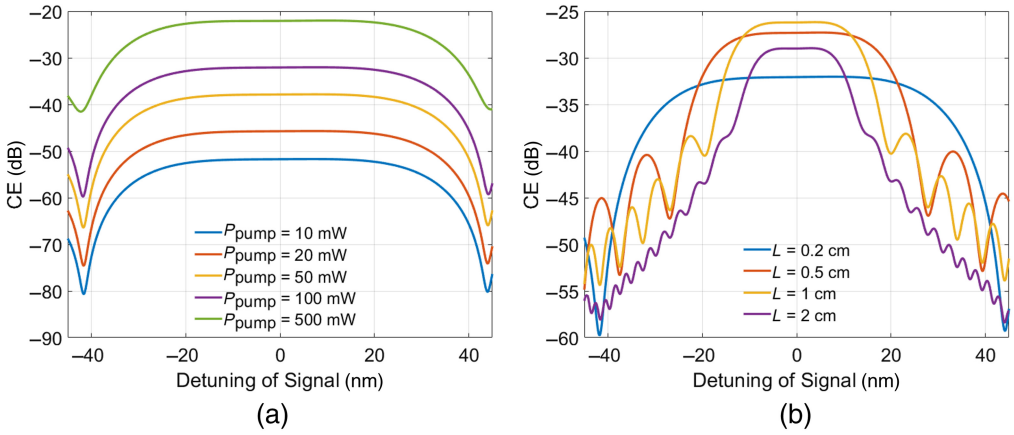

Fig. 9 CE versus detuning of a signal; (a) with different values of pump powers for a waveguide length of 0.2 mm and (b) with different value waveguide lengths for a pump power of 100 mW.

linear propagation loss while maintaining a pump power of 100 mW. As the loss decreases from 5 to 0.5 dB/cm, the optimal length increases from 1 to 7 cm, resulting in an improvement in CE from −26 to −12 dB. Therefore, low-loss waveguides are extremely beneficial for enhancing idler generation efficiency.

All previous simulations have been conducted under the assumption of a phase-matched condition. In practice, the CE exhibits a finite bandwidth, which depends on the dispersion characteristics of the waveguide. As the separation between signal and pump wavelength increases, the CE is impacted due to momentum conservation. For the simulation, the pump wavelength has been chosen at 1550 nm and a 5 dB/cm linear loss of the waveguide is considered. Figure 9(a) shows the CE against signal detuning from the pump for different pump power with a waveguide length of 0.2 cm and geometry of 500 nm × 220 nm. The 3 dB bandwidth is found to be around 56 nm. This bandwidth remains consistent even at higher pump powers, and as shown in earlier simulations, the overall CE improves with increased power levels. Furthermore, Fig. 9(b) illustrates the CE's response to signal detuning for different waveguide lengths for a pump power of 100 mW. As the waveguide length is increased from 0.2 to 2 cm, the bandwidth reduces from 56 to 20 nm. Therefore, the phase matching condition is important to achieve a larger bandwidth for a longer waveguide length. The phase mismatch, induced by wave vectors can be expressed as follows with the help of the Taylor series expression

$$\beta(\omega) = \beta(\omega_p) + \sum_{n=1}^{\infty} \frac{\beta_n}{n!}(\omega - \omega_p)^n, \tag{19}$$

where

$$\beta_n = \left.\frac{\partial^n \beta}{\partial \omega^n}\right|_{\omega=\omega_p}. \tag{20}$$

Therefore,

$$\Delta\beta = \Delta\omega^2 \beta_2 + \frac{1}{12}\Delta\omega^4 \beta_4. \tag{21}$$

The wave vector mismatch is affected by β_2, GVD. The chromatic dispersion (D - ps/nm-km) is related to GVD as

$$D = -\frac{2\pi c}{\lambda^2}\beta_2. \tag{22}$$

Minimizing the dispersion is a crucial aspect of achieving a higher bandwidth of the CE. However, in addition to dispersion, optimizing the effective area (A_{eff}) is also essential, as it directly influences the nonlinearity (γ) of the waveguides. The dispersion and effective areas were simulated using mode solvers for various waveguide widths with two different slab heights:

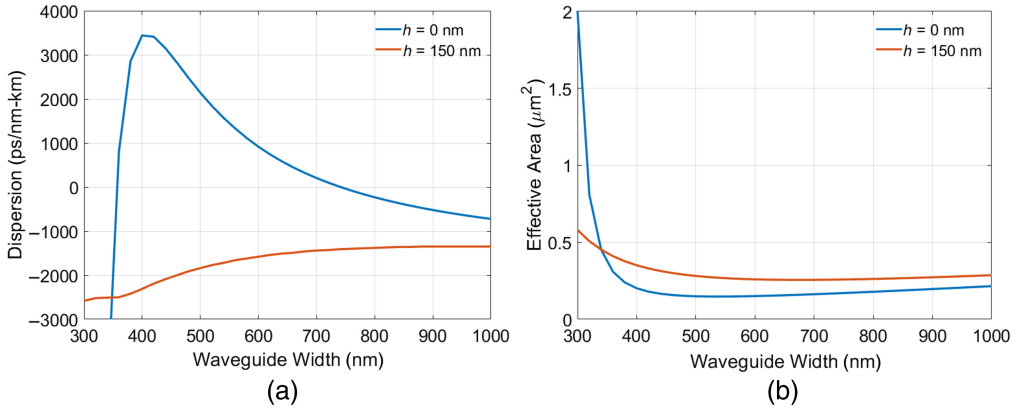

Fig. 10 (a) Dispersion and (b) effective area of the fundamental mode with respect to waveguide width at 1550 nm.

$h = 0$ nm and $h = 150$ nm. As depicted in Fig. 10(a), for $h = 0$ nm, the dispersion crosses zero value at two specific waveguide widths, $W = 350$ nm and $W = 740$ nm. However, the sensitivity of dispersion to changes in waveguide width is smaller for the larger waveguide width of $W = 740$ nm. This characteristic is critical, particularly when considering fabrication-induced uncertainties. Similarly, the effective area of the waveguide is minimized at a waveguide width of 500 nm when the slab height is $h = 0$ nm [refer to Fig. 10(b)]. Therefore, for achieving a larger bandwidth, $W = 740$ nm is the preferable choice, whereas for shorter waveguide lengths and higher CE, $W = 500$ nm stands out as the optimal choice. For experimental demonstration, a 500-nm waveguide width is considered with a length of 2 mm.

3.2 Microring Resonator

The power enhancement inside the microring resonator (MRR) helps to increase the CE. However, due to the power enhancement within the cavity, the various nonlinear effects are visible for a much lower power compared with a straight waveguide. Therefore, in the simulation, the nonlinear effect is considered and compared with the analytical model used in the literature.[16] The top view and the cross-section view of an all-pass MRR are shown in Figs. 11(a) and 11(b), respectively. For a lower effective area, strip ($h = 0$ nm) waveguide geometry has been chosen with a width of 500 nm. The normalized power transmission (T) of an all-pass MRR is given by

$$T = \frac{a^2 + t^2 - 2at\,\cos(\beta L)}{1 + a^2t^2 - 2at\,\cos(\beta L)}, \tag{23}$$

where L is the perimeter of the MRR, a is the round trip coefficient ($\exp(-\alpha L/2)$), and t and k are the through and cross-coupling coefficients. For loss-less directional couplers, $t^2 + k^2 = 1$. The normalized transmission of a 10-μm radius MRR is plotted in Fig. 11(c) for 5 dB/cm propagation loss and cross-coupling coefficient of 0.1. The field enhancement (FE) inside the ring is given by

$$FE = \frac{jk}{1 - t\,\exp(-\alpha L/2 + j\beta L)}. \tag{24}$$

In the vicinity of the resonant wavelength, the normalized transmission and power enhancement have been depicted in Fig. 11(d). It is important to note that, at the resonance wavelength, the power enhancement ($|FE|^2$) inside the resonator is more than 20 dB higher compared to the input power. The CE is given by [16]

$$\eta = |\gamma P_p L'|^2 FE_p^4 FE_s^2 FE_i^2, \tag{25}$$

$$L' = L^2\,\exp(-\alpha L)\frac{1 - \exp(-\alpha L + j\Delta\beta L)}{\alpha L - j\Delta\beta L}, \tag{26}$$

where FE_p, FE_s, and FE_i are the field enhancement inside the MRR corresponding to pump, signal, and idler wavelengths, respectively. This model does not consider the nonlinear effects.

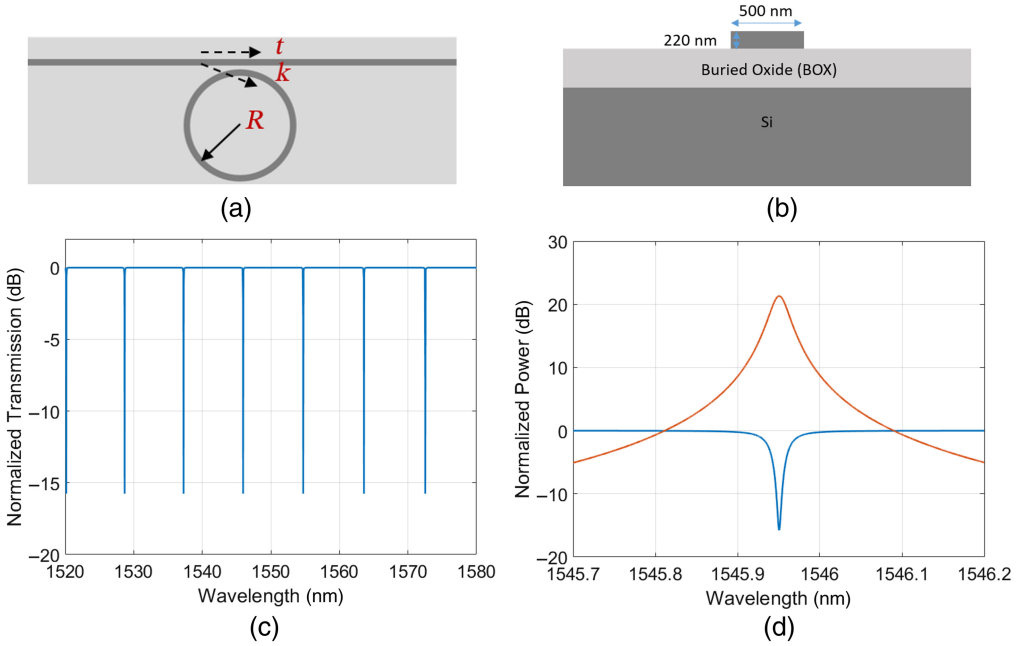

Fig. 11 (a) Top view and (b) cross-section schematic of MRR; (c) normalized transmission spectrum and (d) zoomed view around a resonance along with power enhancement.

However, as the input power increases, the propagation loss and refractive index will be modified. To estimate the CE at higher input power, it is essential to consider the impact of the nonlinearity in the ring resonator. As the input power level increases, the higher power enhancement inside the ring resonator modifies the loss and the refractive index due to the effect of TPA, FCA, and FCD. For the same set of MRR parameters used previously, nonlinear loss and refractive index have been simulated. As shown in Fig. 12, both the loss and refractive index change are much higher in MRR compared to straight waveguides for the same input power level (see Figs. 4 and 5). Therefore, it is important to include the nonlinear effects for the simulation of CE of stimulated FWM in MRR. The pump (A_p), signal (A_s), and idler (A_i) field amplitudes inside the MRR follow the same set of equations [Eqs. (7)–(9)] as for straight waveguides. However, all the field amplitudes need to respect the following boundary conditions at the coupling points ($z = 0$) as depicted in Fig. 13:

$$\begin{bmatrix} P_v^{\text{out}} \\ A_v(0) \end{bmatrix} = \begin{bmatrix} t & -jk \\ -jk & t \end{bmatrix} \begin{bmatrix} P_v^{\text{in}} \\ A_v(L) \end{bmatrix}, \tag{27}$$

where $v = p, s, i$.

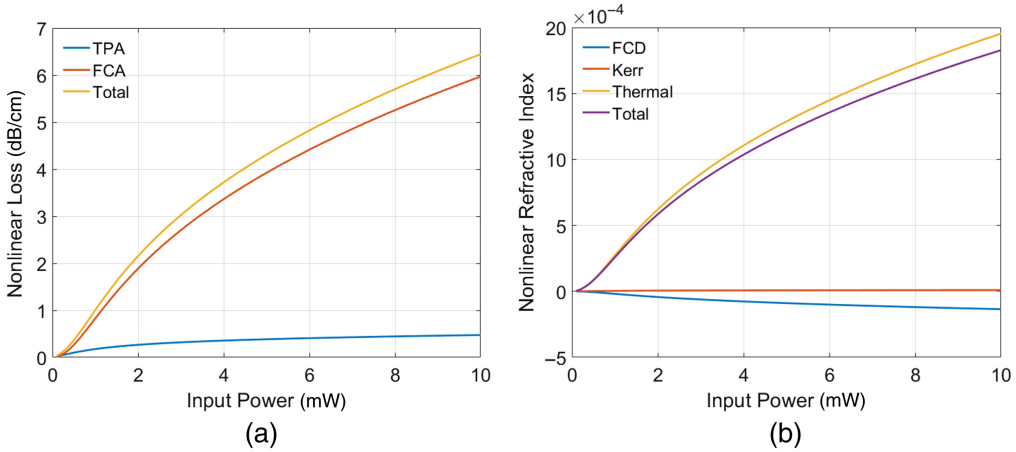

Fig. 12 Nonlinear (a) loss and (b) refractive index change inside the MRR with respect to input power at the bus waveguide.

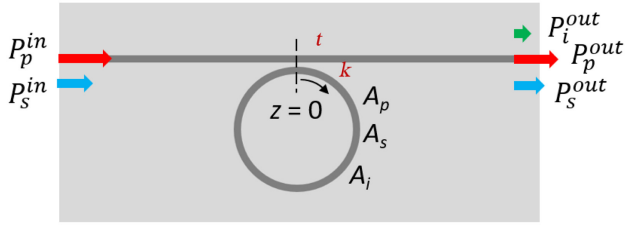

Fig. 13 Stimulated FWM schematic in MRR.

All the coupled equations are solved numerically using MATLAB with the initial and the boundary conditions. For the simulation of CE, the signal power is considered as $P_s^{\text{in}} = -13$ dBm. Results from both the analytical model and numerical model have been plotted in Fig. 13. As the pump power level increases, the CE of the numerical model deviates from the analytical model and saturates at higher power due to nonlinear loss. However, at this power level, the CE is significantly better in MRR compared to a straight waveguide (see Fig. 6).

4 Experimental Results and Discussions

The straight waveguide with 2 mm length and 10 and 20 μm MRRs have been fabricated with different bus to waveguide gaps (G). For the light coupling in and out of straight waveguide and MRR, grating couplers have been integrated at both ends of the devices. To have efficient grating coupling, a slab height of 150 nm is chosen. Therefore two-step lithography is involved to define the straight waveguides and MRRs where there is no slab. The schematic top view of the fabricated devices is shown in Fig. 15 along with the cross-sectional views in two important locations. The devices have been fabricated using in-house silicon photonic technology available at CNNP, IIT Madras. In the first step, grating couplers and waveguides were defined using e-beam lithography, followed by inductively coupled plasma reactive ion etching (ICPRIE) up to h of 150 nm. In the subsequent lithography step, the grating couplers were covered and the sample was etched again to remove the remaining silicon slab. Finally, the e-beam resist hydrogen silsesquioxane (HSQ) was removed by dipping the sample in diluted HF solution. The SEM images of the grating coupler and 20 μm MRR are shown in Fig. 16. The devices were characterized using a high-resolution bandwidth (0.8 pm) optical source spectrum analyzer (OSSA - APEX 2043B) with an optical input power of −6 dBm. The photograph of the experimental setup is shown in Fig. 17. The transmission characteristics (normalized to 0 dBm launched power from OSSA) of the straight waveguide, 10 and 20 μm MRRs are depicted in Fig. 18. A minimum insertion loss of 7 dB is attained at the peak transmission of the grating couplers. The quality factors of the MRRs range between 50,000 and 10,000, corresponding to a waveguide propagation loss of less than 5 dB/cm. The stimulated FWM experiments have been performed in the 2-mm straight waveguide and 20 μm MRR. The experimental setup for stimulated FWM in a straight waveguide of 2 mm length is illustrated in Fig. 19(a). The pump (λ_p) is amplified through

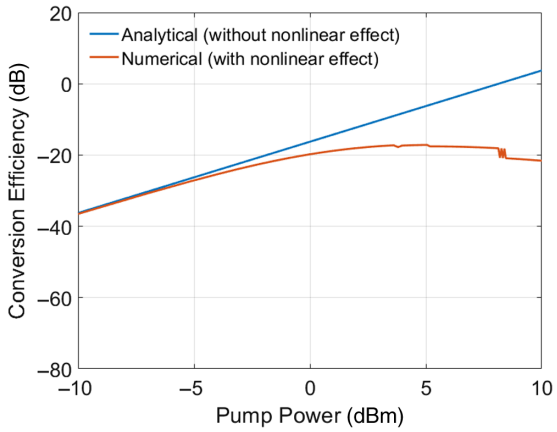

Fig. 14 CE of stimulated FWM in MRR.

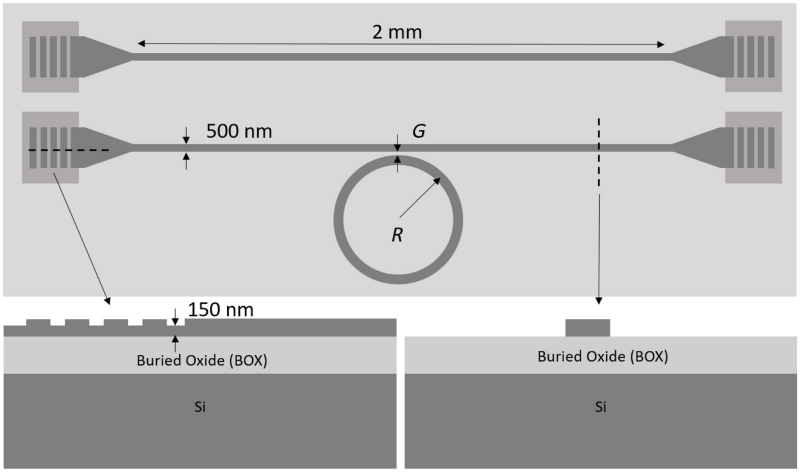

Fig. 15 Layout schematic for device fabrication.

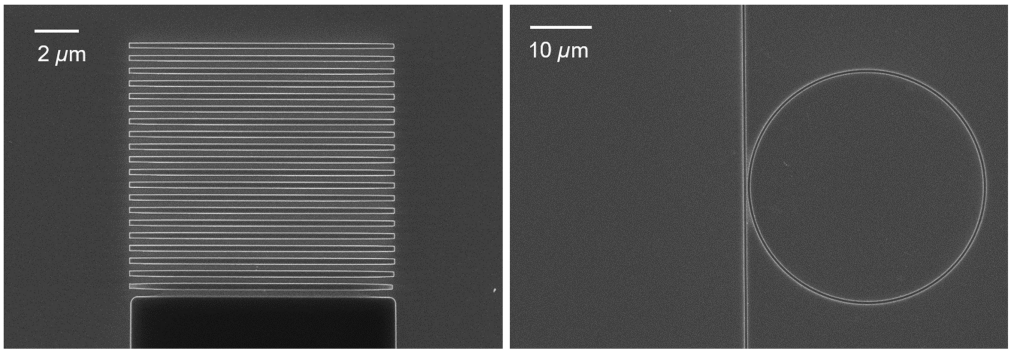

(a) (b)

Fig. 16 SEM images of (a) grating coupler and (b) 20 μm MRR.

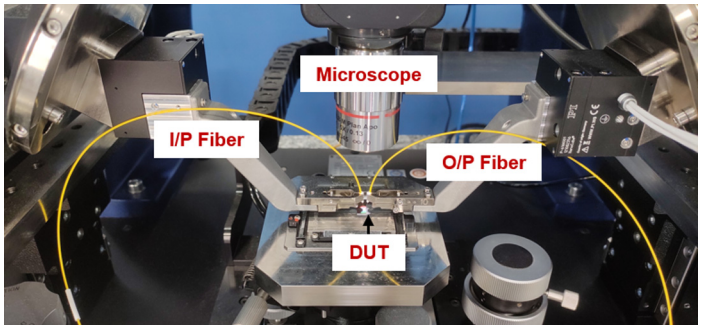

Fig. 17 Image of the experimental setup, used for device characterizations; DUT, device under test; OSSA, optical source spectrum analyzer; I/P, input; and O/P, output.

an erbium-doped fiber amplifier (EDFA) and combined with signal (λ_s) through a 50:50 fiber optic coupler (FOC). Figure 19(b) displays the transmitted FWM spectrum observed in the optical spectrum analyzer (OSA) for pump and signal wavelengths of 1550 and 1545 nm, respectively. The amplified spontaneous emission (ASE) from EDFA increases the noise floor. The launched pump power (P_{in}) after the input grating coupler has been estimated at 12.3 dBm. It is noteworthy that the grating coupling efficiency at signal and idler wavelengths slightly differs. This is taken care of while calculating the CE, which considers idler output at the waveguide with respect to the signal power at the input of the waveguide. The graph in Fig. 19(c) illustrates the conversion efficiencies corresponding to various launched pump powers, maintaining a fixed

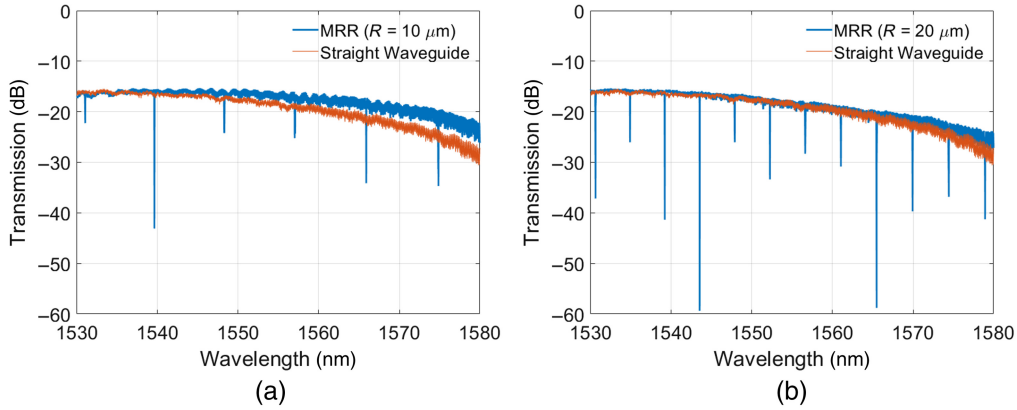

Fig. 18 Normalized transmission characteristics of (a) 10 μm and (b) 20 μm microring resonator along input and output grating couplers.

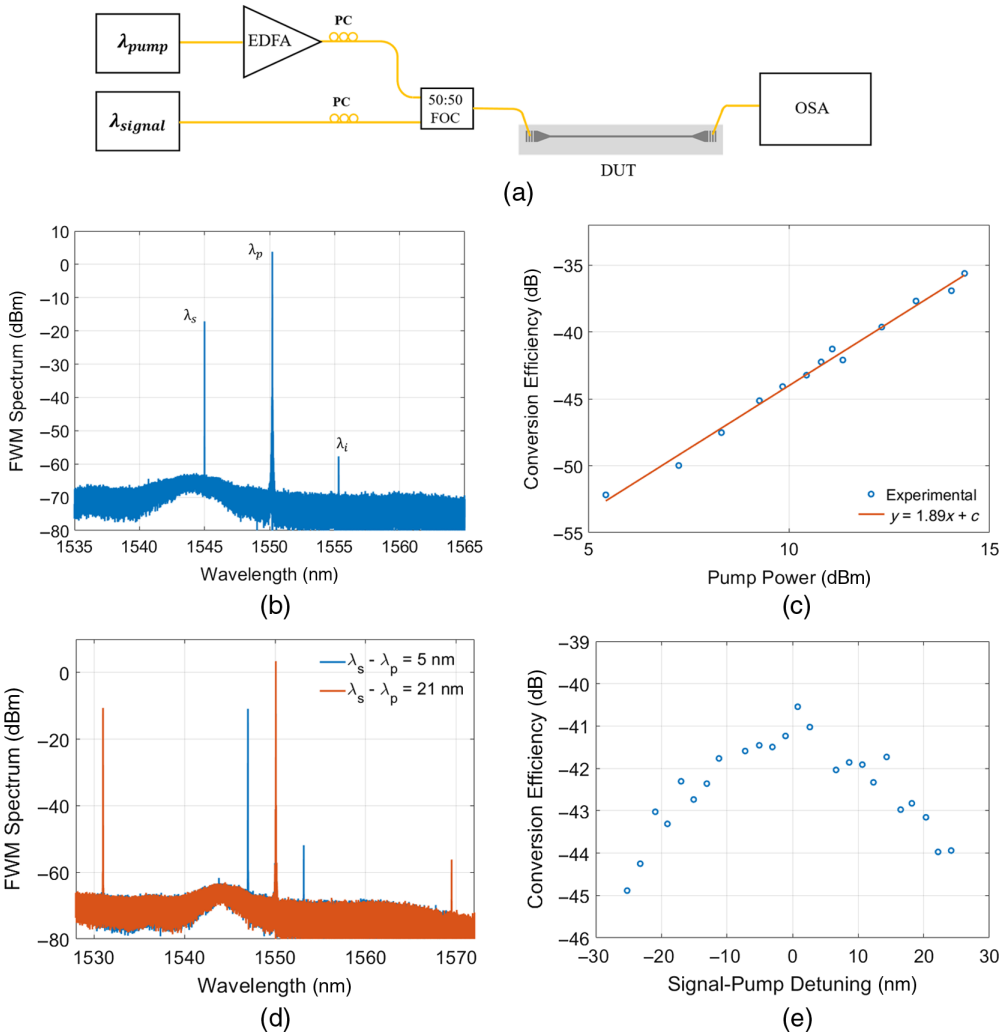

Fig. 19 (a) Experimental set up of stimulated FWM in the straight waveguide, (b) transmitted FWM spectrum in OSA for P_{in} of 9.8 dBm, (c) CE with launched pump power for fixed signal wavelength, (d) two FWM spectra for two different signal wavelengths for fixed pump power and wavelength, and (e) CE for different signal-pump detuning.

signal pump detuning of 5 nm. At a launch pump power of 14.4 dBm, a CE of −35 dB is observed. The fitted curve reveals that CE exhibits an approximate slope of 2 (around 1.89) concerning the pump power in the dB scale. This observation validates the dependence of CE on the square of the pump power. Another aspect of stimulated FWM explores how the CE varies across different signal wavelengths while keeping the pump power and wavelength fixed. The output FWM spectra are depicted for two distinct signal wavelengths in Fig. 19(d), showcasing detunings of 5 and 21 nm from the pump. The pump's wavelength and power remain fixed at 1550 nm and 12.25 dBm, respectively. Furthermore, FWM spectra have been recorded for various signal detunings, and their corresponding CEs are plotted in Fig. 19(e). The 3 dB bandwidth of the CE is over 45 nm around the pump wavelength, which is close to the predicted value (>50 nm) from the theoretical model. However, the peak efficiency (−41 dB) in the measurement is 4 dB higher than the theoretical estimation (−45 dB). This can be attributed primarily to two factors: variation in waveguide geometry that leads to a reduced effective area and underestimation of launched power due to uncertainty about exact coupling in the grating coupler.

To demonstrate stimulated FWM in MRR, the experimental setup has been modified from Fig. 19(a). A narrow passband (0.6 nm) filter (waveshaper) around the pump wavelength was employed to prevent any undesired effect in MRR due to the ASE noise from EDFA. In addition, the laser from the optical source spectrum analyzer (OSSA) has been used as a probe through a 10:90 coupler for aligning the pump to the resonant wavelength. The modified experimental

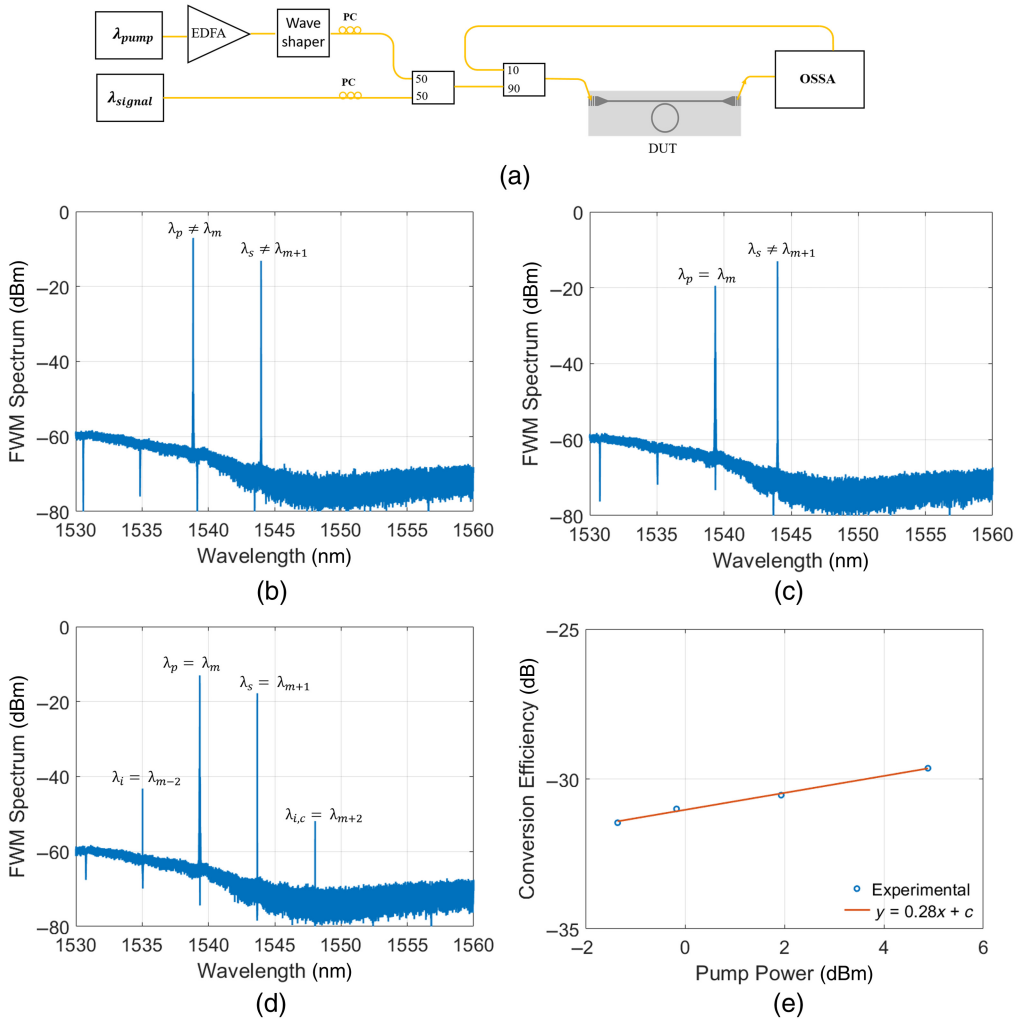

Fig. 20 (a) Experimental setup of stimulated FWM in MRR. Transmitted FWM spectra in OSA: (b) both pump and signal are out of resonances, (c) pump is in resonance while the signal is out of resonance, (d) both pump and signal are in resonances, and (e) CE of stimulated FWM with launched pump power.

setup is depicted in Fig. 20(a). The stimulated FWM has been demonstrated in a 20-μm MRR. When both the pump and signal spectra were outside the resonances of MRR, the idler generation was buried under the low probe power from OSSA [see Fig. 20(b)]. The situation is not improved by aligning only the pump wavelength to the m'th resonance of MRR as shown in Fig. 20(c). However, when both the signal and pump wavelength match with the resonances, there are significant generations of idler (λ_i) and idler conjugate ($\lambda_{i,c}$) corresponding to the $(m-1)$'th and $(m+2)$'th resonances, respectively, as illustrated in Fig. 20(d). The conversion efficiencies, plotted in Fig. 20(e) with respect to the launched pump power levels, deviated from the quadratic behavior as predicted by the simulations shown in Fig. 14. Nevertheless, at this power level, the CE in the MRR is significantly higher compared with the 2-mm straight waveguide, as depicted in Fig. 19(c). These results signify the importance of MRR as nonlinear wave generation with a smaller input power level compared with straight waveguides.

5 Summary and Conclusion

In summary, this paper discussed various nonlinear effects of silicon waveguides with a focus on the TPA effect, followed by FCA and FCD, which significantly influence the FWM process. Nonlinear loss and refractive index depend on the waveguide geometry through the effective area. Simulations of stimulated FWM were conducted based on the coupled equations that consider nonlinear effects and their impact. Furthermore, a detailed approach was taken to simulate the CE of stimulated FWM in both straight waveguides and MRRs. For a particular pump power, there exists an optimum waveguide length beyond which CE degrades. Therefore, to achieve higher CE waveguide propagation loss needs to be improved. For a longer length of the waveguide phase matching also becomes crucial. In the case of MRR, the efficiency is higher for a lower pump power but the nonlinear effects show up at a much lower threshold power compared with the straight waveguide. Therefore, it is important to take into this account while predicting the performance of MRR. Stimulated FWM experiments were performed in 2-mm long waveguides and 20 μm MRRs, where the conversion efficiencies were measured against the launched pump power. For a straight waveguide, a 3-dB bandwidth of close to 35 nm is observed and for a launched pump power of 14.5 dBm, CE is around -35 dB. In the case of 20 μm MRR, we achieved -30 dB CE at a lower pump power of 5 dBm. In summary, our findings demonstrate that MRRs offer superior FWM CE compared with straight waveguides. By comprehensively modeling nonlinear effects, we provide valuable insights into the behavior of stimulated FWM in both structures under high-power conditions. Our findings provide a robust framework for optimizing the FWM process and exploring applications such as frequency comb generation and photon pair generation in the presence of significant nonlinear effects.

Disclosures

The authors declare no conflicts of interest.

Code and Data Availability

Data underlying the results presented in this paper are not publicly available at this time but may be obtained from the authors upon reasonable request.

Acknowledgments

The authors gratefully acknowledge the sponsorship of MeitY, Govt. of India, to establish silicon photonics CoE-CPPICS at IIT Madras.

References

1. S. Y. Siew et al., "Review of silicon photonics technology and platform development," *J. Lightwave Technol.* **39**(13), 4374–4389 (2021).
2. S. Clemmen et al., "Continuous wave photon pair generation in silicon-on-insulator waveguides and ring resonators," *Opt. Express* **17**(19), 16558–16570 (2009).
3. K. Guo et al., "Broadband wavelength conversion in a silicon vertical-dual-slot waveguide," *Opt. Express* **25**(26), 32964–32971 (2017).

4. J. Wang et al., "Multidimensional quantum entanglement with large-scale integrated optics," *Science* **360**(6386), 285–291 (2018).
5. M. A. Foster et al., "Broad-band continuous-wave parametric wavelength conversion in silicon nanowaveguides," *Opt. Express* **15**(20), 12949–12958 (2007).
6. S. Signorini et al., "Intermodal four-wave mixing in silicon waveguides," *Photonics Res.* **6**(8), 805–814 (2018).
7. Q. Lin, O. J. Painter, and G. P. Agrawal, "Nonlinear optical phenomena in silicon waveguides: modeling and applications," *Opt. Express* **15**(25), 16604–16644 (2007).
8. J. R. Ong et al., "Efficient CW four-wave mixing in silicon-on-insulator micro-rings with active carrier removal," *IEEE Photonics Technol. Lett.* **25**, 1699–1702 (2013).
9. M. Borghi, A. Trenti, and L. Pavesi, "Four wave mixing control in a photonic molecule made by silicon microring resonators," *Sci. Rep.* **9**, 408 (2019).
10. G. P. Agrawal, "Nonlinear fiber optics," *Lect. Notes in Phys.* **542**, 195–211 (2000).
11. Y. Guo et al., "The impact of nonlinear losses in the silicon micro-ring cavities on CW pumping correlated photon pair generation," *Opt. Express* **22**(3), 2620–2631 (2014).
12. Z. Wang et al., "The influence of thermal and free carrier dispersion effects on all-optical wavelength conversion in a silicon racetrack-shaped microring resonator," *Laser Phys.* **26**(7), 075403 (2016).
13. A. R. Motamedi et al., "Ultrafast nonlinear optical studies of silicon nanowaveguides," *Opt. Express* **20**(4), 4085–4101 (2012).
14. I. D. Rukhlenko, M. Premaratne, and G. P. Agrawal, "Analytical study of optical bistability in silicon ring resonators," *Opt. Lett.* **35**(1), 55–57 (2010).
15. Q. Xu and M. Lipson, "Carrier-induced optical bistability in silicon ring resonators," *Opt. Lett.* **31**(3), 341–343 (2006).
16. P. Absil et al., "Wavelength conversion in GAAS micro-ring resonators," *Opt. Lett.* **25**(8), 554–556 (2000).

Arnab Goswami received his B.E. degree in electronics and telecommunication engineering from the Indian Institute of Engineering Science and Technology, Shibpur, West Bengal, India, in 2014, and his M.Tech degree in communication engineering from the National Institute of Technology, Agartala, Tripura, India, in 2017. He completed his PhD in the Dept. of Electrical Engineering, IIT Madras, in July 2024. Currently, he serves as Chief Technology Officer at the Centre for Programmable Photonic Integrated Circuits and Systems in the Department of Electrical Engineering, IIT Madras, India.

Yash Raj received his B.Tech degree in electronics and communication engineering from IIT (ISM) Dhanbad in 2021. He is a PhD scholar in the Dept. of Electrical Engineering, IIT Madras. His research interest is programmable integrated photonics.

Bijoy Krishna Das received his master's degree in solid state physics from Vidyasagar University, Midnapore, India, and his PhD (Dr.rer.nat) in integrated optics from the University of Paderborn, Paderborn, Germany. From 1996 to 2006, he was employed in the area of $LiNbO_3$-based integrated optics, which includes 3 years of pre-doctoral research at Microelectronics Center, IIT Kharagpur, India; 4 years of doctoral research with the Department of Applied Physics, University of Paderborn, Germany; and 3 years of postdoctoral research in three different countries (Japan, United States, and Germany). Since August 2006, he has been a professor in the Department of Electrical Engineering, IIT Madras, Chennai, India. His research interests include integrated silicon photonics technology, and he has more than 100 research publications.